



**HAL**  
open science

## **3.4 % solar-to-ammonia efficiency from nitrate using Fe single atomic catalyst supported on MoS<sub>2</sub> nanosheets**

Ji Li, Yuan Zhang, Chao Liu, Lirong Zheng, Eddy Petit, Kun Qi, Yang Zhang, Huali Wu, Wensen Wang, Antoine Tiberj, et al.

### ► To cite this version:

Ji Li, Yuan Zhang, Chao Liu, Lirong Zheng, Eddy Petit, et al.. 3.4 % solar-to-ammonia efficiency from nitrate using Fe single atomic catalyst supported on MoS<sub>2</sub> nanosheets. *Advanced Functional Materials*, Wiley, 2022, 32 (18), pp.2108316. 10.1002/adfm.202108316 . hal-03710525

**HAL Id: hal-03710525**

**<https://hal.archives-ouvertes.fr/hal-03710525>**

Submitted on 30 Jun 2022

**HAL** is a multi-disciplinary open access archive for the deposit and dissemination of scientific research documents, whether they are published or not. The documents may come from teaching and research institutions in France or abroad, or from public or private research centers.

L'archive ouverte pluridisciplinaire **HAL**, est destinée au dépôt et à la diffusion de documents scientifiques de niveau recherche, publiés ou non, émanant des établissements d'enseignement et de recherche français ou étrangers, des laboratoires publics ou privés.

### **3.4 % solar-to-ammonia efficiency from nitrate using Fe single atomic catalyst supported on MoS<sub>2</sub> nanosheets**

*Ji Li, Yuan Zhang, Chao Liu, Lirong Zheng, Eddy Petit, Kun Qi, Yang Zhang, Huali Wu, Wensen Wang, Antoine Tiberj, Xuechuan Wang, Manish Chhowalla, Luc Lajaunie, Ruohan Yu, and Damien Voiry,\**

J. Li, Y. Zhang, X. Wang

College of Bioresources and Materials Engineering, Shaanxi University of Science & Technology, Xi'an 710021, PR China

C. Liu

Shaanxi Collaborative Innovation Center of Industrial Auxiliary Chemistry and Technology, Shaanxi University of Science and Technology, Xi'an 710021, PR China

L. Zheng

Institute of High Energy Physics, Chinese Academy of Science, Beijing 100049, PR China

E. Petit, K. Qi, Y. Zhang, H. Wu, W. Wang, D. Voiry

Institut Européen des Membranes, IEM, UMR 5635, Université Montpellier, ENSCM, CNRS, 34095 Montpellier Cedex 5, France

E-mail: [damien.voiry@umontpellier.fr](mailto:damien.voiry@umontpellier.fr)

A. Tiberj

Laboratoire Charles Coulomb (L2C), Université de Montpellier, CNRS, Montpellier, 34095, France

M. Chhowalla

Department of Materials Science & Metallurgy, University of Cambridge, Cambridge, UK

L. Lajaunie

Instituto Universitario de Investigación de Microscopía Electrónica y Materiales (IMEYMAT), Departamento de Ciencia de los Materiales e Ingeniería Metalúrgica y Química Inorgánica, Facultad de Ciencias, Universidad de Cádiz, Campus Río San Pedro S/N, Puerto Real, 11510, Cádiz, Spain

R. Yu

Nanostructure Research Centre (NRC), Wuhan University of Technology, Wuhan 430070, PR China

Keywords: Fe single-atom catalyst, electrocatalysis, MoS<sub>2</sub> nanosheets, ammonia production

Electrochemical synthesis of NH<sub>3</sub> is a carbon-free alternative to the traditional Haber-Bosch process. Obtaining NH<sub>3</sub> from environmental pollutants, such as nitrates or nitrites, is a more practical route than from the nitrogen reduction reaction (NRR) due to the difficult cleavage of the inert triple bond of nitrogen gas. Here, we report a novel heterogeneous catalyst based on iron (Fe) single-atoms supported on two-dimensional MoS<sub>2</sub> (Fe-MoS<sub>2</sub>) for the nitrate reduction reaction (NO<sub>3</sub>RR). Fe-MoS<sub>2</sub> exhibits remarkable performance with a maximum Faradaic

efficiency of 98 % for  $\text{NO}_3\text{RR}$  to  $\text{NH}_3$  at an onset potential of  $-0.48\text{ V}$  vs. the reversible hydrogen electrode (RHE) as confirmed by our isotopic nuclear magnetic resonance (NMR) analyses. Density functional theory (DFT) calculations reveal that the enhanced selectivity for the production of  $\text{NH}_3$  from single Fe atoms supported on  $\text{MoS}_2$  is attributed to a reduced energy barrier of  $0.38\text{ eV}$  associated with de-oxidation of  $^*\text{NO}$  to  $^*\text{N}$ . We coupled our catalysts to an InGaP/GaAs/Ge triple-junction solar cell to demonstrate a solar-to-ammonia (STA) conversion efficiency of  $3.4\%$  and a yield rate of  $510\ \mu\text{g h}^{-1}\text{ cm}^{-2}$ . Our results open new avenues for design of single-atom catalysts (SAC) for the realization of solar-driven ammonia production.

## 1. Introduction

Ammonia ( $\text{NH}_3$ ) is an important industrial chemical that is widely applied as a nitrogen-rich fertilizer for agriculture, textiles, plastics, and the pharmaceutical industry.<sup>[1,2]</sup> The N cycle perturbation is among the 3 identified planetary boundaries that have already been transgressed by humanity.<sup>[3]</sup> For renewable energy and net-zero carbon emission, ammonia has been identified as a promising energy carrier because of its high hydrogen content of  $17.7\text{ wt}\%$  and its high gravimetric energy density at  $3\text{ kWh kg}^{-1}$ .<sup>[4-7]</sup> The synthesis of  $\text{NH}_3$  via the Haber-Bosch reaction is done under harsh conditions with temperatures and pressures exceeding  $400\text{ }^\circ\text{C}$  and  $200\text{ bar}$ , respectively. With an annual production of  $250\times 10^6$  tons, an estimated amount of  $1\%$  of the world's energy is utilized in the Haber-Bosch, which is responsible for  $1.4\%$  of the global carbon dioxide emissions.<sup>[8-10]</sup> As an alternative, the use of nitrogen and water for the electro-catalytic synthesis of ammonia has recently attracted widespread attention.<sup>[11,12]</sup> However, the direct electrochemical reduction of  $\text{N}_2$  for the production of ammonia under mild conditions is severely limited by several bottlenecks such as: *i*) the high energy barrier required for cleavage of inert  $\text{N}\equiv\text{N}$  triple bond;<sup>[13,14]</sup> *ii*) nonpolar nature of nitrogen molecules that results in a weak interaction between  $\text{N}_2$  and active sites of catalysts;<sup>[15]</sup> *iii*) the very low solubility of  $\text{N}_2$  in water leading to slow reaction rates.<sup>[16,17]</sup>

Alternatively, nitrates ( $NO_3^-$ ) possess unique advantages as nitrogen sources for electrosynthesis of  $NH_3$ . The bond energy of polar  $N=O$  (204 kJ/mol) is four times weaker than the inert non-polar  $N\equiv N$  triple bond, and therefore the  $N=O$  bond can be easily activated at lower energies.<sup>[18]</sup> Nitrate is widely present in the environment and accumulates over time due to agriculture and industrial production activity.<sup>[19,20]</sup>  $NO_3^-$  is a common pollutant of water resources that is responsible for birth defects such as infant methemoglobinemia and blue-baby syndrome as well as thyroid and bladder cancers.  $NO_3RR$  for  $NH_3$  production is therefore not only in line with energy sustainability but is also a pollution mitigation strategy. The electrocatalytic reduction of  $NO_3^-$ -to- $NH_3$  has been reported using Fe,<sup>[21]</sup> Al,<sup>[21]</sup> Cu bulk and nanorods,<sup>[22,23]</sup>  $Cu_2O/Cu$  wires,<sup>[24]</sup> Cu-Ni alloys,<sup>[25]</sup> Cu molecular catalyst,<sup>[17]</sup>  $Co_3O_4$ ,<sup>[26-29]</sup> CoP nanoarray,<sup>[30]</sup>  $Ni_2P$  nanosheets,<sup>[31]</sup> single atom Fe,<sup>[32]</sup> cobalt nano arrays,<sup>[33]</sup> oxide derived cobalt,<sup>[34]</sup> and carbon-based materials.<sup>[35,36]</sup> Improved current density has recently been obtained from cobalt-based electrodes, but they rely on a high loading amount of cobalt. Conversely single atom catalysts (SACs) are anticipated to maximize the atom utilization efficiency of the catalyst but they typically suffer from modest Faradaic efficiencies and/or stability towards the  $NO_3RR$ .

We have recently identified chemically exfoliated  $MoS_2$  nanosheets as two-dimensional electrocatalysts for efficient oxidation of organic sulfides to sulfoxides with near-unity selectivity.<sup>[38]</sup> The nitrate reductase enzyme possesses a Mo (IV) active site coordinated with sulfur coordinating ligands similar to the dimethyl sulfoxide (DMSO) reductase, whereas the nitrogenase is a multinuclear enzyme with  $MoFe_7$  clusters as the active sites. Fe-based catalysts have been reported to be promising for  $NO_3RR$  but the Faradaic efficiency is low because of the competing hydrogen evolution reaction and the formation of nitrogen *via* the five-electron transfer pathway.<sup>[39-41]</sup> To improve the selectivity to  $NO_3^-$ -to- $NH_3$ , Fe single-atom catalysts (SACs) hold promise because the individual Fe atoms possess coordination environment that results in efficient catalytic activity compared to bulk and nanostructured iron. To date, Fe-

SACs have been used in various heterogeneous catalytic reactions, such as CO oxidation,<sup>[42]</sup> oxygen reduction reaction (ORR),<sup>[43–45]</sup> CO<sub>2</sub> reduction reaction (CO<sub>2</sub>RR),<sup>[46,47]</sup> and nitrogen reduction reaction (NRR).<sup>[48,49]</sup>

Inspired by the structure of active sites of enzymes, we report SACs based on individual Fe atoms supported on MoS<sub>2</sub> nanosheets (Fe-MoS<sub>2</sub>) for the electrocatalytic NO<sub>3</sub>RR, which exhibits excellent performance with a Faradaic efficiency of 98 % toward NH<sub>3</sub> at a low overpotential of -0.48 V versus the reversible hydrogen electrode (*vs.* RHE) and a cathodic energy efficiency of 31% at *vs.* RHE and -0.28 V *vs.* RHE, respectively. The optimized Fe-MoS<sub>2</sub> SACs were implemented in a 2-electrode electrolyzer coupled to an external photovoltaic (PV) device to allow solar-driven conversion of **NO<sub>3</sub><sup>-</sup>** to NH<sub>3</sub> to demonstrate a maximum yield rate of 0.03 μmol h<sup>-1</sup> cm<sup>-2</sup> equivalent to 510 μg h<sup>-1</sup> with a near-unity FE for NH<sub>3</sub>. The system achieved stable ammonia production and we estimated the solar-to-ammonia (STA) conversion efficiency to be ca. 3.4 % – setting a new benchmark for the production of NH<sub>3</sub> from a PV-powered electrolyzer based on single atom catalysts.

## 2. Results and Discussion

MoS<sub>2</sub> and Fe-MoS<sub>2</sub> nanosheets were synthesized *via* a hydrothermal reaction using ammonium tetrathiomolybdate: (NH<sub>4</sub>)<sub>2</sub>MoS<sub>4</sub> and iron(III) nitrate nonahydrate as precursors of MoS<sub>2</sub> and Fe, respectively.<sup>[50]</sup> The morphology of as-synthesized Fe-MoS<sub>2</sub> was characterized by scanning electron microscopy (SEM) and transmission electron microscopy (TEM). TEM and SEM revealed the layered structure of the MoS<sub>2</sub> nanosheets (**Figure 1a**), cross-sectional TEM revealed the uniform and continuous coverage of the MoS<sub>2</sub> nanosheets film (thickness ~150 nm) on the conducting carbon cloth (**Figure 1b**). The HAADF-STEM analysis of single-layer catalyst regions shows that the nanosheets are highly crystalline as evidenced by the fast Fourier transform (FFT) patterns in **Figure 1c** and **Figure S1**. The observation along [110] direction of the MoS<sub>2</sub> slabs reveal the presence of the 1T polytype in Fe-MoS<sub>2</sub> in agreement

with the presence of *J* peaks in the Raman spectra (**Figure S2, Table S1**). Energy-dispersive X-ray spectroscopy (EDS) elemental mapping was used to confirm the presence of Fe on MoS<sub>2</sub>. **Figure 1d,e** show uniform distribution of Fe atoms on the nanosheets and no sign of aggregation was observed even at the highest magnification (**Figure S3**). The presence of Fe is also highlighted by spatially-resolved electron energy loss spectroscopy (SR-EELS, **Figure 1f** and **Figure S4**). In particular, the EELS chemical maps evidence that the domain size of Fe is equal or below the EELS voxel size (0.16 nm). It should be noted that the presence of oxygen is also highlighted by EELS and will be discussed later. The high-resolution TEM (HR-TEM) images pointed out that Fe-MoS<sub>2</sub> retains the layered structure of MoS<sub>2</sub> with an interlayer distance of  $\approx 9.1$  Å, ascribed to the (002) crystalline plane (**Figure 1g**). Compared with pristine MoS<sub>2</sub>, the interlayer distance is  $\sim 2.8$  Å larger in the present samples, which is attributed to the presence of Fe atoms on the surface of the nanosheets (**Figure 1g** and **Figure S5**). This observation is further corroborated by our X-ray diffraction (XRD) analyses in which the *d*-spacing of Fe-MoS<sub>2</sub> was found to be 9.8 Å, which is larger than that of MoS<sub>2</sub> at 6.5 Å (**Figure 1h**). We studied the influence of Fe atoms on interlayer spacing by preparing Fe-MoS<sub>2</sub> catalysts with increasing loadings from 1.36 % to 2.14 % (see Supporting Information for details). The position of the (002) did not change significantly with the Fe: Mo ratio suggesting a similar average *d*-space for all Fe-MoS<sub>2</sub> samples. Interestingly the half maximum (FWHM) decreases with the Fe content whereas the intensity of the (002) peak increases; indicating improved stacking order and crystallinity of the MoS<sub>2</sub> nanosheets at higher Fe loadings.<sup>[51]</sup>

Next, we used X-ray photoelectron spectroscopy (XPS) to elucidate the chemical composition of the MoS<sub>2</sub> and Fe-MoS<sub>2</sub> catalysts. The Fe2p spectra of Fe-MoS<sub>2</sub> unambiguously revealed the presence of Fe on the samples. The spectra can be decomposed into two doublets at 707.9/720.8 eV and 709.6/723.2 eV, which are ascribed to contributions from Fe bonded to S and the satellite peaks, respectively (**Figure 1i**).<sup>[52,53]</sup> The splitting of the S2p and Mo3d

spectra (**Figure S6a, b**) for both MoS<sub>2</sub> and Fe-MoS<sub>2</sub> suggests the coexistence of the 1T and the 2H phase MoS<sub>2</sub> in agreement with our Raman and STEM analyses. From the deconvolution of the Mo3d and S2p signals, the amount of 1T phase in MoS<sub>2</sub> and Fe-MoS<sub>2</sub> is estimated to be 42.5 % and 47.0 % respectively, whereas minimal amount of Mo<sup>6+</sup> is detected at 16.9 % and 10.2 %. The presence of an additional doublet at 162.6 eV and 163.9 eV was also identified in the S2p region and attributed to S2p<sub>1/2</sub> and S2p<sub>2/3</sub> signals from S-Fe bond.<sup>[54-56]</sup> X-ray absorption near-edge spectroscopy (XANES) and extended X-ray absorption fine structure (EXAFS) were acquired to elucidate the electronic and coordination structure of Fe-MoS<sub>2</sub>. **Figure 1j** shows the Fe K-edge XANES profiles for Fe-MoS<sub>2</sub>, compared to that of Fe<sub>2</sub>O<sub>3</sub>, FeS, and Fe metal used as references for Fe<sup>3+</sup>, Fe<sup>2+</sup>, and Fe<sup>0</sup>, respectively. The near-edge absorption energy position of Fe-MoS<sub>2</sub> was found to be between that of FeS and Fe<sub>2</sub>O<sub>3</sub>, suggesting that the oxidation state of Fe in Fe-MoS<sub>2</sub> is comprised of between +2 and +3. Only one main peak was visible at 1.78 Å in the Fourier transformed EXAFS (FT-EXAFS) spectrum of Fe-MoS<sub>2</sub> (**Figure 1k**), which is close to that of Fe-S in FeS at 1.87 Å and is attributed to the first coordination shell of Fe-S. It should be noted that no contribution for the Fe-Fe bond expected at ~2.20 Å and ~2.58 Å for Fe<sup>0</sup> and Fe<sup>3+</sup> in Fe metal and Fe<sub>2</sub>O<sub>3</sub> were observed from the FT-EXAFS spectrum. Our X-ray absorption data suggest the fact that Fe is dispersed on the MoS<sub>2</sub> nanosheets at the atomic level. To gain more information on the structural parameters, we performed least-square EXAFS fittings on Fe-MoS<sub>2</sub> (see **Figure S7** and **Table S2**). The corresponding coordination number of Fe atom in the Fe-MoS<sub>2</sub> was estimated to be ≈ 3.5 with the bond lengths of 2.25 Å and 1.97 Å for Fe-S and Fe-O respectively. The identification of the Fe-O bond may be attributed to the presence of axial oxygen atoms bonded to Fe, in good agreement with the observed spatial overlapping of the Fe and O EELS chemical maps (**Figure S4**). All the above results corroborate the single atomic nature of Fe in Fe-MoS<sub>2</sub> catalysts as illustrated in **Figure 1l**.

The electrocatalytic properties of Fe-MoS<sub>2</sub> catalyst for the reduction of NO<sub>3</sub><sup>-</sup> were investigated in an H-cell reactor using a 0.1 M of K<sub>2</sub>SO<sub>4</sub> + 0.1 M NaOH electrolyte solution (See the Methods section for details about the electrochemical measurements). The left panel of **Figure 2a** shows linear sweep voltammetry (LSV) curves measured with and without 0.1 M NaNO<sub>3</sub> for Fe-MoS<sub>2</sub>. We also compared the electrochemical responses of Fe-MoS<sub>2</sub> nanosheets with MoS<sub>2</sub>, Fe foil, carbon cloth used references as well as benchmarked catalysts: Cu, Cu<sub>0.5</sub>Ni<sub>0.5</sub>. Higher current density and lower onset potential were detected in the presence of NO<sub>3</sub><sup>-</sup>. To prove that the change in current density originates from the reduction of NO<sub>3</sub><sup>-</sup> to NH<sub>3</sub> rather than a change in the electrolyte concentration, we estimated the concentration of ammonia after the reaction *via* a colorimetric method using the indophenol blue method (See details in the Supporting Information file and **Figure S8**). Ammonia concentrations were detected in the range of 0.6~2.0 mM after 1 hour of electrolysis under a constant applied potential of -0.48 V versus the reversible hydrogen electrode (*vs.* RHE), which indicates that the change in the LSV data originates from electrocatalytic conversion of NO<sub>3</sub><sup>-</sup>. To exclude contamination that could lead to overestimation of ammonia production, isotopic experiments were conducted using 0.1 M Na<sup>14</sup>NO<sub>3</sub> and 0.1 M Na<sup>15</sup>NO<sub>3</sub>. The <sup>1</sup>H nuclear magnetic resonance (NMR) spectra of the electrolyte after electrolysis are shown in **Figure 2b**. In the case of Na<sup>15</sup>NO<sub>3</sub> electrolyte solution, the <sup>1</sup>H NMR spectrum exhibits two clear symmetric signals at  $\delta = 7.02$  and  $7.14$  ppm with a spacing of 73.1 Hz assigned to <sup>15</sup>NH<sub>3</sub>, due to scalar interaction between <sup>1</sup>H and <sup>15</sup>N. Conversely, in presence of Na<sup>14</sup>NO<sub>3</sub> three symmetric signals located at 6.99, 7.08, and 7.17 ppm were detected with a spacing of 52.2 Hz ascribed to <sup>14</sup>NH<sub>3</sub>.<sup>[12]</sup> We performed a blank experiment in the absence of NO<sub>3</sub><sup>-</sup> and no signals from <sup>15</sup>NH<sub>3</sub> nor <sup>14</sup>NH<sub>3</sub> were detected. Overall, our results confirmed the successful reduction of NO<sub>3</sub><sup>-</sup> to NH<sub>3</sub> and rule out contamination. The content of ammonia in the electrolyte was further quantified *via* <sup>1</sup>H NMR using an external standard for calibration (**Figure S9**). The ammonia quantification using <sup>1</sup>H NMR and colorimetry are comparable and validates our colorimetric strategy for the

quantification of the Faradaic efficiency of the reaction on Fe-MoS<sub>2</sub> (**Table S4**). **Figure 2c** shows the Faradaic efficiency for the formation of NH<sub>3</sub> on Fe-MoS<sub>2</sub> compared to pristine MoS<sub>2</sub>, Cu, and Cu<sub>50</sub>Ni<sub>50</sub> alloy used as the benchmarked catalyst for the NO<sub>3</sub>RR. We noted that Cu, and Cu<sub>50</sub>Ni<sub>50</sub> were prepared and tested according to previous reports from the literature, although we could not achieved the same level of performance.<sup>[25]</sup> The selectivity of Fe-MoS<sub>2</sub> nanosheets rapidly increases with the onset potential and the Faradaic efficiency for NH<sub>3</sub> reaches a maximum value of 95.8% at -0.48 V vs. RHE, which is higher than that for MoS<sub>2</sub> nanosheets and Cu at 40.8 % and 22.5 % respectively. We also tested other possible products including NO<sub>2</sub><sup>-</sup>, NH<sub>2</sub>NH<sub>2</sub>, NH<sub>2</sub>OH and N<sub>2</sub> using gas chromatography (GC) and NMR. NH<sub>2</sub>NH<sub>2</sub>, NH<sub>2</sub>OH, and N<sub>2</sub> were not found, while nitrite and hydrogen were detected at low and large overpotentials, respectively (**Figure S10**). The enhanced FE on Fe-MoS<sub>2</sub> translates to a specific current density  $j_{\text{NH}_3}$  of -8.4 mA cm<sup>-2</sup>, which represents 7.1- and 2.8-fold increase compared to MoS<sub>2</sub> and Cu, respectively. The onset potential for NO<sub>3</sub>RR – measured at -1 mA cm<sup>-2</sup> – was found to be ≈ 100 mV vs. RHE for Fe-MoS<sub>2</sub>, while the absence of Faradaic current below 100 mV vs. RHE revealed the absence of electrochemical reactions. For comparison, we determined the onset potential for MoS<sub>2</sub> and Fe to be 200 mV and 40 mV vs. RHE, respectively (**Figure 2d**). The  $j_{\text{NH}_3}$  and onset potential on Fe-MoS<sub>2</sub> are comparable with those from Cu<sub>50</sub>Ni<sub>50</sub> alloy. To further quantify the catalytic properties of Fe-MoS<sub>2</sub>, we estimated the cathodic energy efficiency ( $EE_{\text{NO}_3\text{RR}}$ ) of the different catalysts. The  $EE_{\text{NO}_3\text{RR}}$  for Fe-MoS<sub>2</sub> was found to be the highest at 31 % for a cathodic potential of -0.28 V vs. RHE, which is at least 4 times higher than that of MoS<sub>2</sub>, Cu, and Cu<sub>50</sub>Ni<sub>50</sub> alloy (**Figure 3b**). These results also compared favorably with previous reports from the literature based on CuNi alloy,<sup>[57]</sup> Cu nanosheets,<sup>[58]</sup> Cu/CuO nanowire arrays,<sup>[59]</sup> titanium electrode,<sup>[60]</sup> and copper-molecular solid catalyst (**Table S5**),<sup>[17]</sup> and other MoS<sub>2</sub>-based catalysts those we synthesized (**Figure S11**). Our investigations indicate that the presence of atomically dispersed Fe on the two-dimensional MoS<sub>2</sub> matrix enhances

both the intrinsic catalytic activity and the selectivity with respect to  $H_2$ .

We then sought to better understand the behavior of Fe-MoS<sub>2</sub> by exploring the influence of Fe loading and the nitrate concentration in the electrolyte. At -0.48 V vs. RHE, the Faradaic efficiency continuously increases from 30.1 % up to 95.8 % as the Fe content is increased from 0 % (i.e. pristine MoS<sub>2</sub>) to 2.13% (**Figure S12a,b**). The effect of nitrate concentration on catalytic properties was explored by varying the  $NO_3^-$  concentration from 10 mM up to 100 mM. Remarkably we observed that the FE for NH<sub>3</sub> on Fe-MoS<sub>2</sub> is largely maintained in presence of diluted  $NO_3^-$  and the FE remains as high as 70% for a nitrate concentration as low as 10 mM. On the contrary, the concentration profoundly affects the NO<sub>3</sub>RR performance of MoS<sub>2</sub> and the FE decreases to ~3.8 % for a nitrate concentration of 10 mM (**Figure 2e**). This apparent 18-fold increase of  $FE_{NH_3}$  in dilute medium highlights the high selectivity of Fe-MoS<sub>2</sub> towards the NO<sub>3</sub>RR versus the competing hydrogen evolution reaction (HER).

We assessed the charge transfer resistance ( $R_{CT}$ ) at the interface between Fe-MoS<sub>2</sub> and the electrolyte using electrochemical impedance spectroscopy (EIS) (**Figure S13a**). The Nyquist plots of different catalysts exhibit the typical semicircle shape, which reflects the interface resistance on the electrode surface. By modeling the EIS responses with the Randles equivalent circuit, the values of  $R_{CT}$  are found to be low in the case of Fe-MoS<sub>2</sub> at 13.1  $\Omega$  compared to 24.8  $\Omega$  for MoS<sub>2</sub> and 9.8  $\Omega$  for Cu. This points to faster kinetics for electron transfer at the surface of the catalyst in agreement with the reduction of the Tafel slope at 260 mV dec<sup>-1</sup> compared to >500 mV dec<sup>-1</sup> for pristine MoS<sub>2</sub> and other Cu-based catalysts (**Figure S13b**). We conclude that the reduced  $R_{CT}$  and Tafel slope result from improved conductivity of the Fe-MoS<sub>2</sub> nanosheets and the presence of the metallic 1T polytype within the MoS<sub>2</sub> lattice. To evaluate the stability toward the conversion of  $NO_3^-$  to NH<sub>3</sub>, we applied a steady-state potential on the Fe-MoS<sub>2</sub> electrode, while recording the current density and measuring the FE using colorimetry. **Figure 2f** shows that the FE at -0.48 V vs. RHE displays minimal changes

over 7 hours with an average value of 98 %. The robustness of the Fe-MoS<sub>2</sub> performance was further corroborated by the high retention of the current density, showing that the 7-hour average of yield rate was 431.8±38.6 μg h<sup>-1</sup> cm<sup>-2</sup>. Finally, to confirm the stability of the Fe single atoms, we measured the content in Fe in the electrolyte after 6 cycles of 1 hour of electrolysis. The Fe concentration was found to be below the detection limit of 2 ppb, suggesting limited leaching of Fe atoms during NO<sub>3</sub>RR (**Table S6**).

We explored the isotopic effect on the NO<sub>3</sub>RR by investigating the electrochemical responses of Fe-MoS<sub>2</sub> in presence of Na<sup>14</sup>NO<sub>3</sub> and Na<sup>15</sup>NO<sub>3</sub> respectively.<sup>[61]</sup> Using Na<sup>15</sup>NO<sub>3</sub>, we observe a decrease in the current density together with an increase of the overpotential of ~40 mV (**Figure 3a**). The LSV and chronoamperometry responses were recorded for each nitrate isotope with increasing temperatures from 25 °C to 65 °C and the apparent activation energies were obtained by fitting the *Arrhenius* plot of the specific current density  $j_{\text{NH}_3}$  as a function of  $T^{-1}$  (**Figure 3a**). The slope of the *Arrhenius* plot was estimated to be 0.18 and 0.21 for Na<sup>14</sup>NO<sub>3</sub> and Na<sup>15</sup>NO<sub>3</sub> respectively. The apparent difference between the two isotopes is in agreement with the change in the polarization curves and is attributed to the slow diffusion of Na<sup>15</sup>NO<sub>3</sub> in the Helmholtz layer as well as in the interlayer of Fe-MoS<sub>2</sub> nanosheets.

To obtain more insight into the remarkable selectivity of the Fe-MoS<sub>2</sub> for the electrosynthesis of NH<sub>3</sub>, we investigated NO<sub>3</sub>RR on different MoS<sub>2</sub>-based SACs with different transition metals. **Figure S14** shows the polarization curves on Co-MoS<sub>2</sub>, Ni-MoS<sub>2</sub>, Cu-MoS<sub>2</sub>, and Fe-MoS<sub>2</sub> nanosheets in the presence of NO<sub>3</sub><sup>-</sup>. Fe-MoS<sub>2</sub> outperformed the other MoS<sub>2</sub> SACs as evidenced by the larger current density and the lower onset potential compared to Co-MoS<sub>2</sub>, Ni-MoS<sub>2</sub>, Cu-MoS<sub>2</sub>. The FE for NH<sub>3</sub> was found to be 59.6 % at -0.3 V vs. RHE on Co-MoS<sub>2</sub>, which is lower than that of Fe-MoS<sub>2</sub> at 86.4 % (**Figure 3c**). Remarkably the values of the onset potential for NO<sub>3</sub>RR and  $j_{\text{NH}_3}$  on Fe-MoS<sub>2</sub> are also 4~10 folds higher and at least 400 mV vs. RHE lower than other MoS<sub>2</sub> catalysts (**Figure 3d**) – strongly suggesting that the dispersed Fe

atoms on the MoS<sub>2</sub> nanosheets are key for enhancing the intrinsic catalytic activity and selectivity towards the NO<sub>3</sub>RR.

To rationalize our experimental results, we conducted density functional theory calculations to investigate the NO<sub>3</sub>RR on the different single-atom catalysts supported on MoS<sub>2</sub>. The structural models of SACs consisted of four different transition metals: Fe, Co, Ni, and Cu atoms coordinated with 3 sulfur atoms as presented in **Figure S15**.<sup>[62]</sup> **Figure 4a** shows the successive steps associated with nitrate reduction on the MoS<sub>2</sub> SACs, which can be decomposed into two main electrochemical processes: \*NO<sub>3</sub><sup>-</sup> → \*NO<sub>2</sub> → \*NO → \*N and \*NH → \*NH<sub>2</sub> → \*NH<sub>3</sub> corresponding to the deoxidation and hydrogenation mechanisms, respectively.<sup>[23,63]</sup> There is a general agreement that the catalytic active sites of MoS<sub>2</sub> are located at the edges of the nanosheets.<sup>[64]</sup> We first computed the Gibbs free energy of the full NO<sub>3</sub>RR pathway on different MoS<sub>2</sub> SACs. On pristine MoS<sub>2</sub>, the first deoxidation step: \*NO<sub>3</sub><sup>-</sup> → \*NO<sub>2</sub> is considered as the potential-dependent step (PDS) with a very high reaction free energy of 1.47 eV. Such a high value is attributed to the formation of strong covalent bonds between two adjacent Mo atoms and two oxygen atoms of NO<sub>3</sub><sup>-</sup> (with  $\Delta E_{\text{NO}_3^-} = -4.04$  eV for the largest charge transfer of 0.85 e<sup>-</sup>) (**Figure S16**). Conversely, all SACs display a different energy profile illustrating that the inclusion of metallic single atoms profoundly modifies the thermodynamics landscape of the NO<sub>3</sub>RR on MoS<sub>2</sub>. The PDS step is associated with the \*NO deoxidation step (see **Figure 4c**). Among the different metal single atoms, the lowest reaction free energy is obtained for Fe-MoS<sub>2</sub> at 0.38 eV – in qualitative agreement with our experimental observations. When plotting the energy barrier for the reaction as function of the experimental onset potential, we observed a linear relationship, which clearly suggests that the catalytic activity of MoS<sub>2</sub> SACs is controlled by the barrier of the deoxidation step (**Figure 4d**). To confirm the high selectivity towards the formation of ammonia, we calculated the energy profiles for the formation of NO<sub>2</sub>, NO and N<sub>2</sub> on Fe-MoS<sub>2</sub>. According to our DFT predictions, the energy barrier associated with the formation of NO<sub>2</sub>, NO, N<sub>2</sub>O, and N<sub>2</sub> are estimated to be 2.01 eV,

3.05 eV, 0.82eV and 0.70 eV respectively (**Figure S17**). These values are clearly larger than the barrier associated with the formation of  $\text{NH}_3$ , which suggests a high selectivity towards the formation of ammonia on Fe-MoS<sub>2</sub> in agreement with our experimental data.

To elucidate the origin of the reduced energy barrier for the PDS on the active sites, we examined the projected densities of states (PDOS) of NO adsorption on Fe-MoS<sub>2</sub> (**Figure S18**). We found that there is a strong overlap between energy levels of the  $\alpha$ -spin and  $\beta$ -spin  $d$  orbitals of Fe-MoS<sub>2</sub> and the  $\pi^*$  orbitals of NO, which leads to an orbital splitting and rearrangement to form new  $d$ - $\pi^*$  bonding and antibonding orbitals (**Figure 4b**). According to our calculations of the adsorption energy of \*NO on the MoS<sub>2</sub> SACs ( $E_{\text{ads, NO}}$ ), we identified the following trend:  $E_{\text{ads, NO}}(\text{Fe-MoS}_2) > E_{\text{ads, NO}}(\text{Co-MoS}_2) > E_{\text{ads, NO}}(\text{Ni-MoS}_2) > E_{\text{ads, NO}}(\text{Cu-MoS}_2)$  (**Figure S19** and **Table S8**). Our results suggest that the stabilization of \*NO on Fe-MoS<sub>2</sub> enhances the catalytic activity – in agreement with the Brønsted–Evans–Polanyi (BEP) relation that has been proposed to describe multi-step processes (see Supporting Information). To visualize the bonding situations between the active site and the N atom of NO, we employed the Crystal Orbital Hamiltonian Populations (COHP) analysis,<sup>[65,66]</sup> which is a theoretical method for partitioning the band-structure energy into orbital-pair interactions. The integrated projected COHP (IpCOHP) below the Fermi level provides qualitative estimation of the bond strength. Usually, the bonding state is characterized by a positive overlap population that leads to negative Hamiltonian off-site elements that contribute to increasing the interactions between adsorbates and the catalyst surface. A comparison of the COHP curves for the four different catalysts (as seen in **Figure 4e**) reveals that a significant number of antibonding states of M-N interactions (with M and N being the transition metal atom and the N atom in NO) are below the Fermi level of the Ni-MoS<sub>2</sub> and Cu-MoS<sub>2</sub>. Conversely, fewer antibonding states of M-N are present below the Fermi levels of the Fe-MoS<sub>2</sub> and Co-MoS<sub>2</sub>, which indicates that there is a larger orbital overlap between the  $d$  band of the catalyst and the  $2\pi^*$  of \*NO and a lower electron density in the antibonding orbitals below the Fermi level in both Fe-MoS<sub>2</sub> and the Co-MoS<sub>2</sub>. The IpCOHP

between Fe and N for Fe-MoS<sub>2</sub> was found to be -2.74 eV more negative than the other three MoS<sub>2</sub> SACs suggesting that stabilization of \*NO intermediate is responsible for the reduction of the barrier for the formation of the \*N intermediate associated with the PDS step of the reaction.

To evaluate the potential of Fe-MoS<sub>2</sub> for practical ammonia production devices, we integrated the catalysts in a two-electrode H-cell reactor powered by an external photovoltaic (PV) cell. **Figure 5a** shows the respective polarization curves of the cathode and the anode measured in a 3-electrode configuration. The onset potentials for the NO<sub>3</sub>RR and OER – measured by definition at 1 mA cm<sup>2</sup> were estimated to be -0.13 V and 2.06 V vs. RHE, respectively, giving an onset potential of 2.2 V for the full cell. **Figure 5b** presents the electrocatalytic response of the electrolyzer for applied potentials between 0 to 5.0 without compensating for internal resistance. The 2-electrode electrolyzer exhibited an onset potential of 2.26 V consistent with the value predicted from our 3-electrode experiments. We then evaluated the electrolysis property of the full cell, while the Faradaic efficiency was systematically measured at increasing cell voltage. The Faradaic efficiency for NH<sub>3</sub> continuously increased up to 4 V to approach a near-unity value. **Figures 5c,d** summarize the full cell energy efficiency (EE), the yield rate, EPC, and the electric power consumption (EPC, in kWh kg<sup>-1</sup>) obtained by varying the voltage. The EE<sub>full-cell</sub> was estimated to be 24.2 %, which indicates that our Fe-MoS<sub>2</sub> nanosheets possess a high conversion capability from electric to chemical energy. In addition, the EPC was found to be 46.6 kWh kg<sup>-1</sup> at 4.0 V while the yield rate reaches a value of 0.024 mmol h<sup>-1</sup> cm<sup>-2</sup> equivalent to 412.6 μg h<sup>-1</sup> cm<sup>-2</sup>. We coupled the 2-electrode H-cell reactor with a PV cell to achieve indirect photocatalytic conversion of nitrate to ammonia. The relatively large potential associated with the electrochemical synthesis of ammonia typically makes the combination of PV and electrolysis processes difficult to realize experimentally at reasonable efficiencies. A GaInAs/Ga(In)As/Ge triple-junction solar cell was used to generate sufficient photovoltage to drive the catalytic reaction. As presented in **Figure**

**5d** and **Figure S20**, the negative and positive poles were connected with wires to the Fe-MoS<sub>2</sub> cathode and Pt anodes, respectively, and the solar cell was illuminated by standard AM 1.5G spectrum (100 mW cm<sup>-2</sup>) provided by a Xe solar simulator. **Figure 5e** presents the J–V characteristic curve of the tandem cell under 1 sun, yielding a  $V_{OC}$  of  $\approx 5$  V while exhibiting a solar-to-electric power conversion efficiency (PCE) of 29.89 %. To accurately calculate the solar-to-ammonia (STA) conversion efficiency, the LSV curve of the full cell was measured. The size of the electrodes was adjusted in order to minimize the energy loss of the PV-driven electrolysis. We estimated the energy loss between the PV and the PV-electrolysis systems to be only 4.25 % (**Figure S21**). The operating point was determined from the intersection of the J–V curves of both the solar cell and the H-cell reactor.<sup>[67]</sup> The results show that the current density and the cell tension at the operating point reached  $\sim 7.19$  mA cm<sup>-2</sup> and 4.02 V respectively as shown by the red point in **Figure 5e**. Using the thermodynamic potential of the reaction, the electrolysis current, and the Faradaic efficiency (See Supporting information for details about the calculations), we estimated the STA efficiency to be  $\sim 3.9$  %. To confirm the accuracy of the predicted operating point, we also measured the photocurrents from the NO<sub>3</sub>RR process in an unbiased light-driven configuration (**Figure 5f**). The operating point of the NO<sub>3</sub>RR was close to the maximum power point (MPP) of the solar panel tandem cell (7.06 mA cm<sup>-2</sup> at  $V_{MP}=4.23$  V) (the orange point in **Figure 5e**). We performed solar-driven electrolysis of nitrate for 1 hour and the amount of NH<sub>3</sub> was estimated to reach 60.7  $\mu$ mol; equivalent to a concentration of 1.02 mM or 17.3 ppm – larger the contamination threshold of  $\approx 1$  ppm.<sup>[12]</sup> The photocatalytic activity corresponds to a yield rate of  $\sim 0.03$  mmol h<sup>-1</sup> cm<sup>-2</sup>, equivalent to 510  $\mu$ g h<sup>-1</sup> cm<sup>-2</sup>, which outperforms the previous report on the photocatalysis of the NO<sub>3</sub>RR. The estimated STA efficiency was found to be  $\sim 3.4$  %, which is among the highest ever reported and sets a new benchmark for solar-driven ammonia production based on single atom catalysts (**Table S9**).<sup>[34]</sup>

### 3. Conclusion

In summary, we have designed a Fe single-atomic catalyst on two-dimensional MoS<sub>2</sub> nanosheets for electrocatalytic conversion of nitrate to ammonia. Fe-MoS<sub>2</sub> catalysts exhibit excellent NO<sub>3</sub>RR properties with Faradaic efficiency as high as 98 % for production of NH<sub>3</sub> at a low overpotential of < -0.5 V vs. RHE and a cathodic energy efficiency of 31 % at -0.28 V vs. RHE. The excellent activity and selectivity of Fe-MoS<sub>2</sub> are supported by DFT analysis, which confirmed the superior ability of individual Fe atoms on MoS<sub>2</sub> to activate NO<sub>3</sub><sup>-</sup> due to the strong interaction between 2π\* orbital of NO species and *d* band orbitals of Fe atoms that leads to low energy barrier for the limiting \*NO to \*N reaction. We integrated Fe-MoS<sub>2</sub> in a two-electrode H cell reactor coupled to a PV cell and achieved a solar-to-ammonia conversion efficiency of ca. 3.4 % with a yield rate of 510 μg h<sup>-1</sup> cm<sup>-2</sup>. Our investigation sheds light on a practical strategy for the realization of PV-electrolysis systems for the production of ammonia and opens up future applications for solar-driven NH<sub>3</sub> production.

### **Supporting Information**

Supporting Information is available from the Wiley Online Library or from the author.

### **Acknowledgements**

D.V. acknowledges funding from the European Research Council (ERC) under the European Union's Horizon 2020 research and innovation program (grant agreement No 804320).

The authors acknowledge the use of TEM instrumentation provided by the National Facility ELECM I ICTS ("Division de Microscopia Electronica", Universidad de Cadiz, DME-UCA).

LL acknowledges funding from the Andalusian regional government (FEDER-UCA-18-106613), the European Union's Horizon 2020 research and innovation program (grant agreement 823717 – ESTEEM3) and the Spanish Ministerio de Economía y Competitividad (PID2019-107578GA-I00).

J. L. acknowledges financial support from the National Science Foundation of China (Grant No. 21808134) and start-up funding from Shaanxi University of Science & Technology.

This work was supported by the Fundamental Research Funds for the Central Universities (WUT: 2019III012GX, 2020III002GX). Part of the S/TEM investigations was performed at the Nanostructure Research Center (NRC), which is supported by the State Key Laboratory of Advanced Technology for Materials Synthesis and Processing, and the State Key Laboratory of Silicate Materials for Architectures (all of the laboratories are at the Wuhan University of Technology). The authors also acknowledge the use of (S)TEM instrumentation provided by the National Facility ELECMI ICTS ("Division de Microscopia Electronica", Universidad de Cadiz, DME-UCA).

### **Conflict of Interest**

The authors declare no conflict of interest

### References

- [1] V. Rosca, M. Duca, M. T. de Groot, M. T. M. Koper, *Chem. Rev.* **2009**, *109*, 2209.
- [2] W. Guo, K. Zhang, Z. Liang, R. Zou, Q. Xu, *Chem. Soc. Rev.* **2019**, *48*, 5658.
- [3] W. Steffen, K. Richardson, J. Rockström, S. E. Cornell, I. Fetzer, E. M. Bennett, R. Biggs, S. R. Carpenter, W. De Vries, C. A. De Wit, C. Folke, D. Gerten, J. Heinke, G. M. Mace, L. M. Persson, V. Ramanathan, B. Reyers, S. Sörlin, *Science (80-. )*. **2015**, *347*, DOI 10.1126/science.1259855.
- [4] R. Schlögl, *Angew. Chemie Int. Ed.* **2003**, *42*, 2004.
- [5] M. D. Fryzuk, *Nature* **2004**, *427*, 498.
- [6] J. Guo, P. Chen, *Chem* **2017**, *3*, 709.

- [7] C. He, Z. Y. Wu, L. Zhao, M. Ming, Y. Zhang, Y. Yi, J. S. Hu, *ACS Catal.* **2019**, *9*, 7311.
- [8] X. Chen, N. Li, Z. Kong, W.-J. Ong, X. Zhao, *Mater. Horizons* **2018**, *5*, 9.
- [9] I. Rafiqul, C. Weber, B. Lehmann, A. Voss, *Energy* **2005**, *30*, 2487.
- [10] D. Bao, Q. Zhang, F. L. Meng, H. X. Zhong, M. M. Shi, Y. Zhang, J. M. Yan, Q. Jiang, X. B. Zhang, *Adv. Mater.* **2017**, *29*, 1.
- [11] Y. Luo, G. F. Chen, L. Ding, X. Chen, L. X. Ding, H. Wang, *Joule* **2019**, *3*, 279.
- [12] S. Z. Andersen, V. Čolić, S. Yang, J. A. Schwalbe, A. C. Nielander, J. M. McEnaney, K. Enemark-Rasmussen, J. G. Baker, A. R. Singh, B. A. Rohr, M. J. Statt, S. J. Blair, S. Mezzavilla, J. Kibsgaard, P. C. K. Vesborg, M. Cargnello, S. F. Bent, T. F. Jaramillo, I. E. L. Stephens, J. K. Nørskov, I. Chorkendorff, *Nature* **2019**, *570*, 504.
- [13] R. Shi, Y. Zhao, G. I. N. Waterhouse, S. Zhang, T. Zhang, *ACS Catal.* **2019**, *9*, 9739.
- [14] Q. Qin, T. Heil, M. Antonietti, M. Oschatz, *Small Methods* **2018**, *2*, 1800202.
- [15] J. Zhang, Y. Ji, P. Wang, Q. Shao, Y. Li, X. Huang, *Adv. Funct. Mater.* **2020**, *30*, 1906579.
- [16] L. Zeng, X. Li, S. Chen, J. Wen, F. Rahmati, J. van der Zalm, A. Chen, *Nanoscale* **2020**, *12*, 6029.
- [17] G.-F. Chen, Y. Yuan, H. Jiang, S.-Y. Ren, L.-X. Ding, L. Ma, T. Wu, J. Lu, H. Wang, *Nat. Energy* **2020**, *5*, 605.
- [18] A. Stirling, I. Pápai, J. Mink, D. R. Salahub, *J. Chem. Phys.* **1994**, *100*, 2910.
- [19] R. K. Rai, D. Tyagi, S. K. Singh, *Eur. J. Inorg. Chem.* **2017**, *2017*, 2450.
- [20] S. Xu, D. C. Ashley, H.-Y. Kwon, G. R. Ware, C.-H. Chen, Y. Losovyj, X. Gao, E. Jakubikova, J. M. Smith, *Chem. Sci.* **2018**, *9*, 4950.
- [21] W. Li, C. Xiao, Y. Zhao, Q. Zhao, R. Fan, J. Xue, *Catal. Letters* **2016**, *146*, 2585.
- [22] T. Wu, X. Kong, S. Tong, Y. Chen, J. Liu, Y. Tang, X. Yang, Y. Chen, P. Wan, *Appl. Surf. Sci.* **2019**, *489*, 321.

- [23] D. Reyter, G. Chamoulaud, D. Bélanger, L. Roué, *J. Electroanal. Chem.* **2006**, 596, 13.
- [24] Y. Wang, W. Zhou, R. Jia, Y. Yu, B. Zhang, *Angew. Chemie Int. Ed.* **2020**, 59, 5350.
- [25] Y. Wang, A. Xu, Z. Wang, L. Huang, J. Li, F. Li, J. Wicks, M. Luo, D.-H. Nam, C.-S. Tan, Y. Ding, J. Wu, Y. Lum, C.-T. Dinh, D. Sinton, G. Zheng, E. H. Sargent, *J. Am. Chem. Soc.* **2020**, 142, 5702.
- [26] L. Su, K. Li, H. Zhang, M. Fan, D. Ying, T. Sun, Y. Wang, J. Jia, *Water Res.* **2017**, 120, 1.
- [27] J. Gao, B. Jiang, C. Ni, Y. Qi, Y. Zhang, N. Oturan, M. A. Oturan, *Appl. Catal. B Environ.* **2019**, DOI 10.1016/j.apcatb.2019.05.016.
- [28] C. Li, K. Li, C. Chen, Q. Tang, T. Sun, J. Jia, *Sep. Purif. Technol.* **2020**, 237, 116485.
- [29] Y. Wang, C. Liu, B. Zhang, Y. Yu, *Sci. China Mater.* **2020**, 63, 2530.
- [30] G. Wen, J. Liang, Q. Liu, T. Li, X. An, F. Zhang, A. A. Alshehri, K. A. Alzahrani, Y. Luo, Q. Kong, X. Sun, *Nano Res. 2021* **2021**, 1.
- [31] G. Wen, J. Liang, L. Zhang, T. Li, Q. Liu, X. An, X. Shi, Y. Liu, S. Gao, A. M. Asiri, Y. Luo, Q. Kong, X. Sun, *J. Colloid Interface Sci.* **2022**, 606, 1055.
- [32] Z.-Y. Wu, M. Karamad, X. Yong, Q. Huang, D. A. Cullen, P. Zhu, C. Xia, Q. Xiao, M. Shakouri, F.-Y. Chen, J. Y. (Timothy) Kim, Y. Xia, K. Heck, Y. Hu, M. S. Wong, Q. Li, I. Gates, S. Siahrostami, H. Wang, *Nat. Commun. 2021 121* **2021**, 12, 1.
- [33] X. Deng, Y. Yang, L. Wang, X.-Z. Fu, J.-L. Luo, X. Deng, L. Wang, -Z X Fu, J.-L. Luo, Y. Yang, *Adv. Sci.* **2021**, 8, 2004523.
- [34] N. C. Kani, J. A. Gauthier, A. Prajapati, J. Edgington, I. Bordawekar, W. Shields, M. Shields, L. C. Seitz, A. R. Singh, M. R. Singh, *Energy Environ. Sci.* **2021**, DOI 10.1039/d1ee01879e.
- [35] M. Ghazouani, H. Akrouf, L. Bousselmi, *Desalin. Water Treat.* **2014**, 1.
- [36] J. Ding, W. Li, Q.-L. Zhao, K. Wang, Z. Zheng, Y.-Z. Gao, *Chem. Eng. J.* **2015**, 271, 252.

- [37] Y. Wang, A. Xu, Z. Wang, L. Huang, J. Li, F. Li, J. Wicks, M. Luo, D. H. Nam, C. S. Tan, Y. Ding, J. Wu, Y. Lum, C. T. Dinh, D. Sinton, G. Zheng, E. H. Sargent, *J. Am. Chem. Soc.* **2020**, *142*, 5702.
- [38] L. Maachou, K. Qi, E. Petit, Z. Qin, Y. Zhang, D. Cot, V. Flaud, C. Reibel, H. El-Maghrbi, L. Li, P. Miele, D. Kaplan, M. Chhowalla, N. Onofrio, D. Voiry, *J. Mater. Chem. A* **2020**, *8*, 25053.
- [39] W. Teng, N. Bai, Y. Liu, Y. Liu, J. Fan, W. X. Zhang, *Environ. Sci. Technol.* **2018**, *52*, 230.
- [40] G. You, C. Wang, J. Hou, P. Wang, Y. Xu, L. Miao, J. Liu, *Chem. Eng. J.* **2021**, *419*, 129646.
- [41] Z. Liu, S. Dong, D. Zou, J. Ding, A. Yu, J. Zhang, C. Shan, G. Gao, B. Pan, *Water Res.* **2020**, *173*, 115596.
- [42] B. L. He, J. S. Shen, Z. X. Tian, *Phys. Chem. Chem. Phys.* **2016**, *18*, 24261.
- [43] D. Liu, J. Li, S. Ding, Z. Lyu, S. Feng, H. Tian, C. Huyan, M. Xu, T. Li, D. Du, P. Liu, M. Shao, Y. Lin, *Small Methods* **2020**, *4*, 1900827.
- [44] C. Zhu, Q. Shi, B. Z. Xu, S. Fu, G. Wan, C. Yang, S. Yao, J. Song, H. Zhou, D. Du, S. P. Beckman, D. Su, Y. Lin, *Adv. Energy Mater.* **2018**, *8*, 1801956.
- [45] M. Xiao, J. Zhu, L. Ma, Z. Jin, J. Ge, X. Deng, Y. Hou, Q. He, J. Li, Q. Jia, S. Mukerjee, R. Yang, Z. Jiang, D. Su, C. Liu, W. Xing, *ACS Catal.* **2018**, *8*, 2824.
- [46] H. Zhang, J. Li, S. Xi, Y. Du, X. Hai, J. Wang, H. Xu, G. Wu, J. Zhang, J. Lu, J. Wang, *Angew. Chemie Int. Ed.* **2019**, *58*, 14871.
- [47] S. Vijay, J. A. Gauthier, H. H. Heenen, V. J. Bukas, H. H. Kristoffersen, K. Chan, *ACS Catal.* **2020**, *10*, 7826.
- [48] F. Lü, S. Zhao, R. Guo, J. He, X. Peng, H. Bao, J. Fu, L. Han, G. Qi, J. Luo, X. Tang, X. Liu, *Nano Energy* **2019**, *61*, 420.

- [49] L. Zhang, M. Cong, X. Ding, Y. Jin, F. Xu, Y. Wang, L. Chen, L. Zhang, *Angew. Chemie* **2020**, *132*, 10980.
- [50] L. Zhang, X. Ji, X. Ren, Y. Ma, X. Shi, Z. Tian, A. M. Asiri, L. Chen, B. Tang, X. Sun, *Adv. Mater.* **2018**, *30*, 1800191.
- [51] J. Yang, A. R. Mohmad, Y. Wang, R. Fullon, X. Song, F. Zhao, I. Bozkurt, M. Augustin, E. J. G. Santos, H. S. Shin, W. Zhang, D. Voiry, H. Y. Jeong, M. Chhowalla, *Nat. Mater.* **2019**, *18*, 1309.
- [52] B. Tang, Z. G. Yu, H. L. Seng, N. Zhang, X. Liu, Y.-W. Zhang, W. Yang, H. Gong, *Nanoscale* **2018**, *10*, 20113.
- [53] M. Li, H. Du, L. Kuai, K. Huang, Y. Xia, B. Geng, *Angew. Chemie* **2017**, *129*, 12823.
- [54] X. Chen, N. C. Berner, C. Backes, G. S. Duesberg, A. R. McDonald, *Angew. Chemie Int. Ed.* **2016**, *55*, 5803.
- [55] Y. Shi, Y. Wang, J. I. Wong, A. Yuan, S. Tan, C.-L. Hsu, L.-J. Li, Y.-C. Lu, & Hui, Y. Yang, H. Y. Y. ( Yanghuiying@, **2013**, DOI 10.1038/srep02169.
- [56] R. Wang, M. Yan, H. Li, L. Zhang, B. Peng, J. Sun, D. Liu, S. Liu, *Adv. Mater.* **2018**, *30*, 1800618.
- [57] Y. Wang, A. Xu, Z. Wang, L. Huang, J. Li, F. Li, J. Wicks, M. Luo, D. H. Nam, C. S. Tan, Y. Ding, J. Wu, Y. Lum, C. T. Dinh, D. Sinton, G. Zheng, E. H. Sargent, *J. Am. Chem. Soc.* **2020**, DOI 10.1021/jacs.9b13347.
- [58] X. Fu, X. Zhao, X. Hu, K. He, Y. Yu, T. Li, Q. Tu, X. Qian, Q. Yue, M. R. Wasielewski, Y. Kang, *Appl. Mater. Today* **2020**, DOI 10.1016/j.apmt.2020.100620.
- [59] Y. Wang, W. Zhou, R. Jia, Y. Yu, B. Zhang, *Angew. Chemie - Int. Ed.* **2020**, *59*, 5350.
- [60] J. M. McEnaney, S. J. Blair, A. C. Nielander, J. A. Schwalbe, D. M. Koshy, M. Cargnello, T. F. Jaramillo, *ACS Sustain. Chem. Eng.* **2020**, DOI 10.1021/acssuschemeng.9b05983.

- [61] N. Dubouis, C. Yang, R. Beer, L. Ries, D. Voiry, A. Grimaud, *ACS Catal.* **2018**, *8*, 828.
- [62] T. Yang, T. T. Song, J. Zhou, S. Wang, D. Chi, L. Shen, M. Yang, Y. P. Feng, *Nano Energy* **2020**, *68*, 104304.
- [63] J.-X. Liu, D. Richards, N. Singh, B. R. Goldsmith, *ACS Catal.* **2019**, *9*, 7052.
- [64] G. Li, D. Zhang, Q. Qiao, Y. Yu, D. Peterson, A. Zafar, R. Kumar, S. Curtarolo, F. Hunte, S. Shannon, Y. Zhu, W. Yang, L. Cao, *J. Am. Chem. Soc.* **2016**, *138*, 16632.
- [65] R. Dronskowski, P. E. Blöchl, *J. Phys. Chem.* **1993**, *97*, 8617.
- [66] R. Nelson, C. Ertural, J. George, V. L. Deringer, G. Hautier, R. Dronskowski, *J. Comput. Chem.* **2020**, *41*, 1931.
- [67] L. Jingshan, I. Jeong-Hyeok, M. T. Mayer, S. Marcel, N. Mohammad Khaja, P. Nam-Gyu, T. S David, F. H. Jin, G. Michael, *Science (80-. )*. **2014**.

## Figures

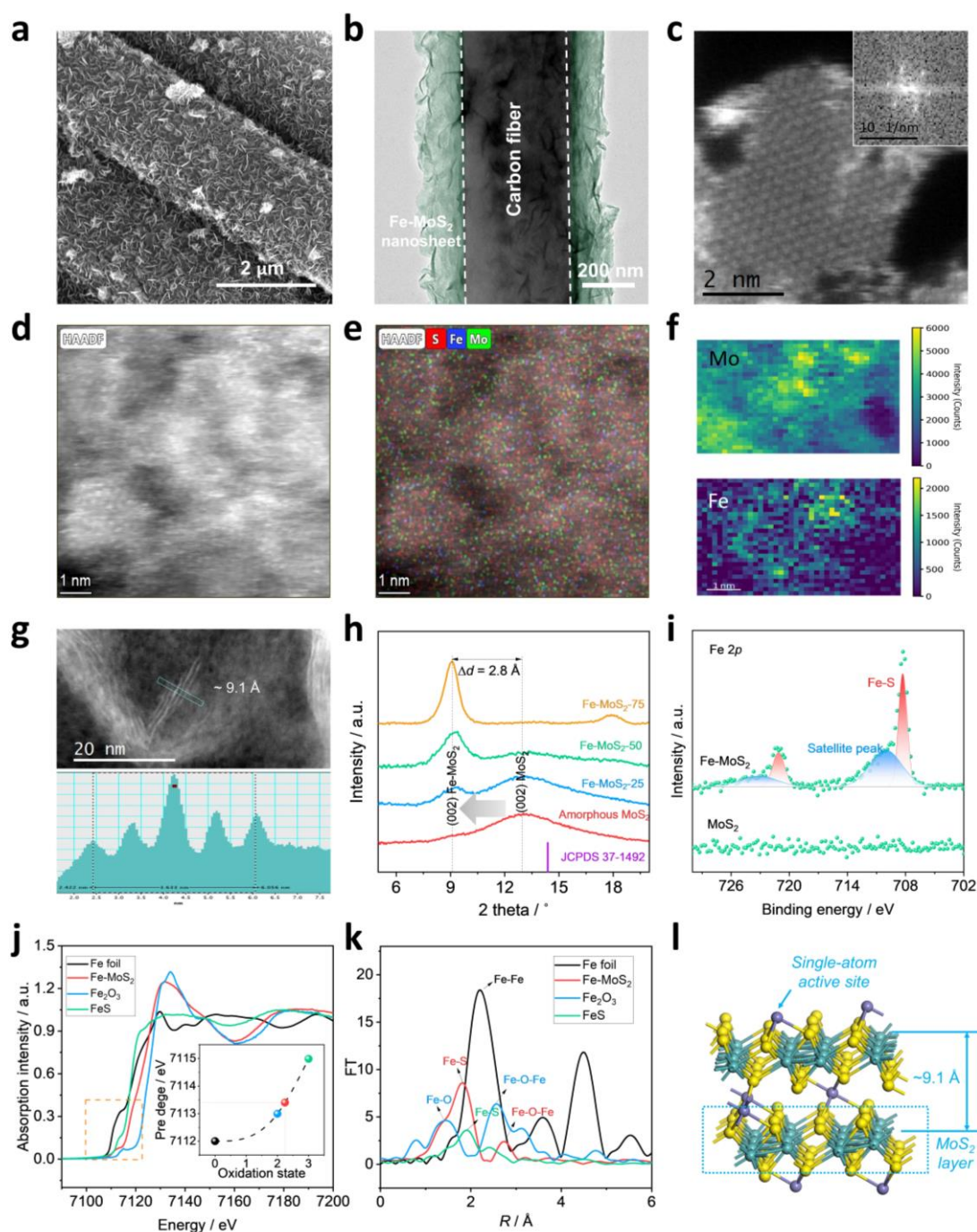


**Figure 1 | The physical characterizations of Fe-MoS<sub>2</sub>.** a,b, Scanning electron microscopy (SEM) and transmission electron microscopy (TEM) images of the Fe-MoS<sub>2</sub> nanosheets grown on the carbon support. c,d, High-angle annular dark-field imaging scanning transmission electron microscopy (HAADF-STEM) image of Fe-MoS<sub>2</sub> nanosheets. Inset: corresponding diffraction pattern confirming the single-crystalline nature of the nanosheet. e,f, High resolution TEM (HRTEM) - energy dispersive X-ray analyses (EDX) and electron energy loss (EELS) elemental mapping images of Fe-MoS<sub>2</sub> nanosheets. g, HR-STEM image of the interlayer

spacing of Fe-MoS<sub>2</sub> and the corresponding line profiles showing an average d-spacing of  $\approx 9.1$  Å. **h**, X-ray diffraction (XRD) patterns of the Fe-MoS<sub>2</sub> nanosheets with different iron content and compared to pristine MoS<sub>2</sub>. **i**, High resolution Fe2p XPS spectra for Fe-MoS<sub>2</sub> and MoS<sub>2</sub>. **j**, Normalized XANES spectra and **k**, Fourier transform magnitudes in *R* space of the EXAFS at the Fe K edge of Fe-MoS<sub>2</sub> nanosheets, Fe<sub>2</sub>O<sub>3</sub>, FeS, and Fe foil, **l**, Proposed structure of Fe-MoS<sub>2</sub>.

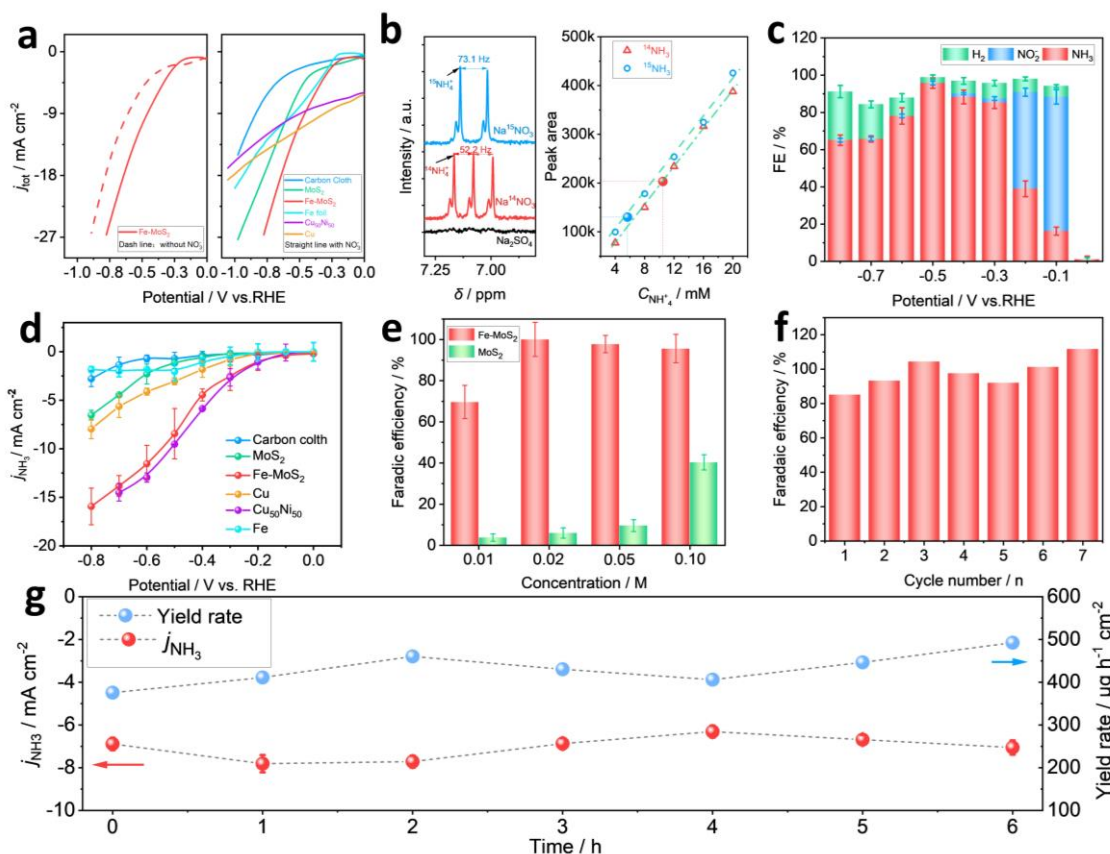


**Figure 2 | The electrochemical performance investigation for NO<sub>3</sub>RR on Fe-MoS<sub>2</sub>.** **a, Left:** Linear sweep voltammetry (LSV) curves of Fe-MoS<sub>2</sub> nanosheets with and without 0.1 M NaNO<sub>3</sub> electrolyte. **Right:** LSV curves of Fe-MoS<sub>2</sub> nanosheets, MoS<sub>2</sub> nanosheets, Fe foil, carbon cloth and benchmarked catalysts: Cu, Cu<sub>0.5</sub>Ni<sub>0.5</sub> in presence of 0.1 M NaNO<sub>3</sub>. **b, Left:** <sup>1</sup>H nuclear magnetic resonance (NMR) spectra (600 MHz) of electrolyte produced from NO<sub>3</sub>RR under -0.58 V vs. RHE using 0.1 M Na<sup>14</sup>NO<sub>3</sub> and Na<sup>15</sup>NO<sub>3</sub> as N source. **Right:** Calibration curve of <sup>14</sup>NH<sub>4</sub>Cl and <sup>15</sup>NH<sub>4</sub>Cl measured by <sup>1</sup>H NMR (right). The experimental NO<sub>3</sub>RR results are shown as solid symbols. **c,** Potential-dependent Faradaic efficiency of ammonia on Fe-MoS<sub>2</sub>, MoS<sub>2</sub>, Cu, Fe foil, compared with the carbon support. **d,** Evolution of the specific current density:  $j_{\text{NH}_3}$  as a function of the potential (vs. RHE). **e,** Comparison of the Faradaic efficiency for ammonia on the Fe-MoS<sub>2</sub> and MoS<sub>2</sub> nanosheets at different nitrate concentrations measured at an applied potential of -0.48 V vs. RHE. **f,** Evolution of the Faradaic efficiency at -0.48 V over 7 cycles of 1 hour. The electrolyte was refreshed for every cycle. **g,** Evolution of  $j_{\text{NH}_3}$  and the yield rate of Fe-MoS<sub>2</sub> nanosheets over time.

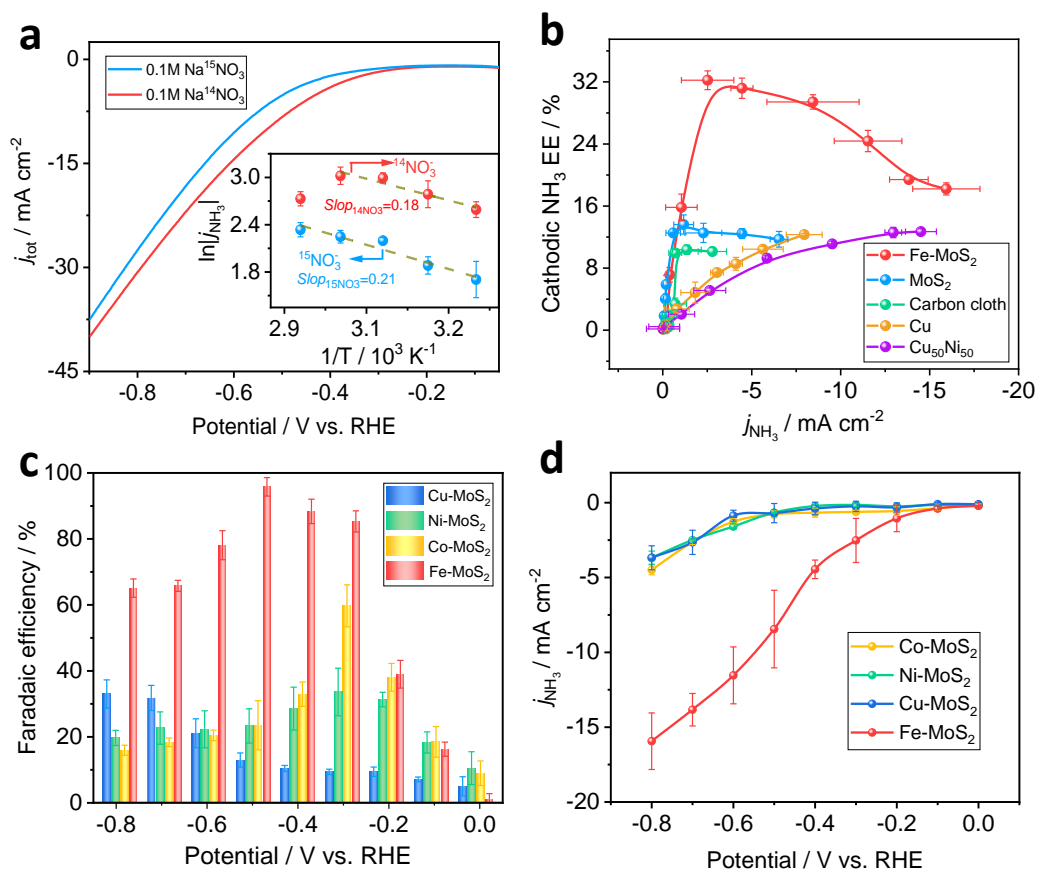


**Figure 3 | The electrochemical performance towards NO<sub>3</sub>RR on MoS<sub>2</sub>-based SACs. a,** Linear scanning voltammetry (LSV) and Arrhenius plots (inset) of Fe-MoS<sub>2</sub> measured in Na<sup>14</sup>NO<sub>3</sub> and Na<sup>15</sup>NO<sub>3</sub> at different temperatures. **b,** The cathodic energy efficiency (EE) for NO<sub>3</sub><sup>-</sup>-to-NH<sub>3</sub> conversion on Fe-MoS<sub>2</sub> and MoS<sub>2</sub> nanosheets compared with Cu, Cu<sub>50</sub>Ni<sub>50</sub>, and the carbon support. **c,** Potential-dependent Faradaic efficiency for ammonia on Cu-MoS<sub>2</sub>, Ni-MoS<sub>2</sub>, Co-MoS<sub>2</sub> and Fe-MoS<sub>2</sub> nanosheets. **d,** Evolution of  $j_{\text{NH}_3}$  on Co-MoS<sub>2</sub>, Ni-MoS<sub>2</sub>, and Cu-MoS<sub>2</sub> nanosheets as a function of the applied potential.

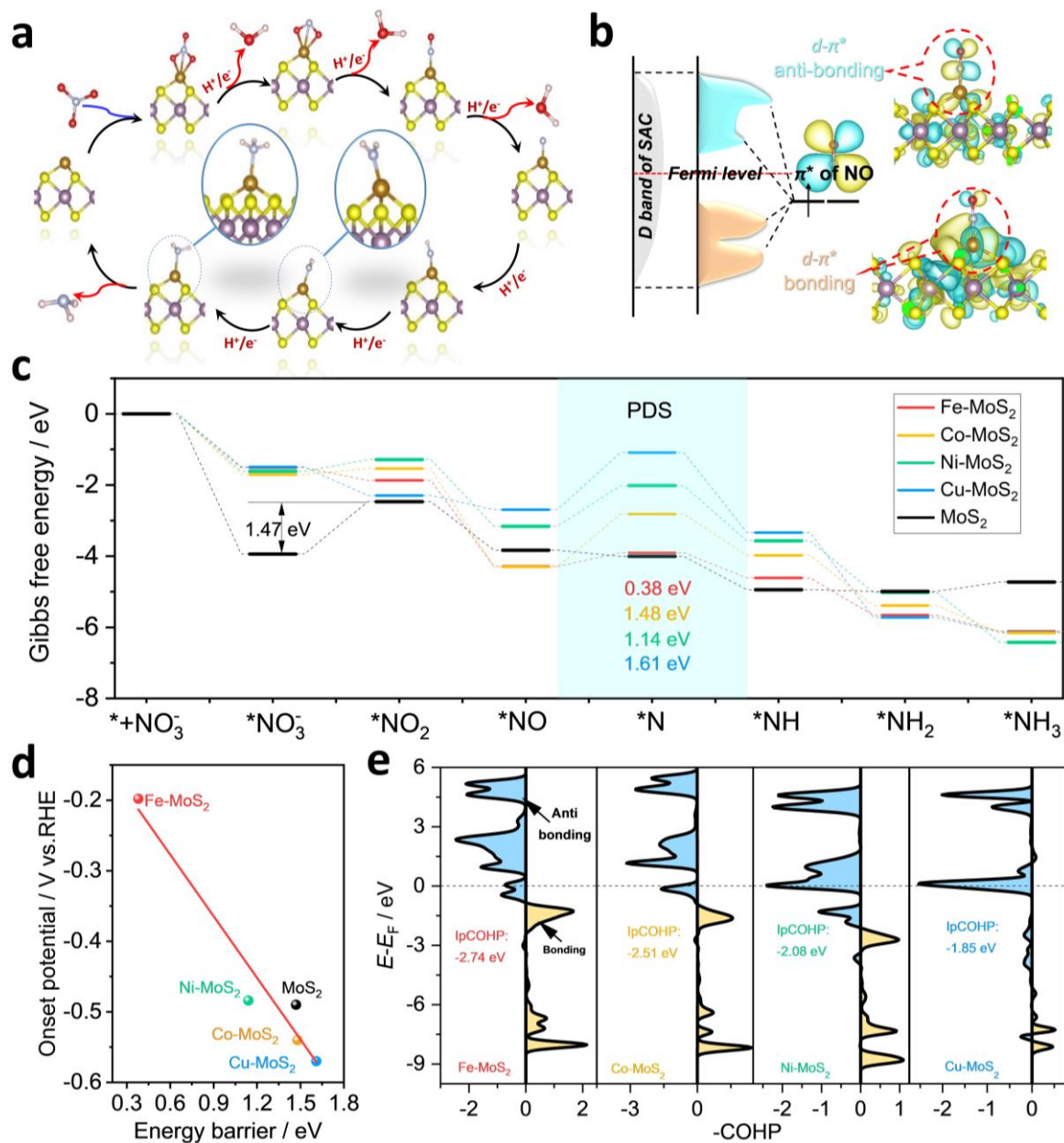


**Figure 4 | DFT calculations of the NO<sub>3</sub>RR on MoS<sub>2</sub> SACs. a**, Reaction pathway for the NO<sub>3</sub>RR on M-MoS<sub>2</sub> nanosheets (M: Fe, Co, Ni, and Cu, respectively). **b**, Schematic diagram of the interaction between NO and the M-MoS<sub>2</sub> nanosheets. **c**, Reaction Gibbs free energies for different intermediates on M-MoS<sub>2</sub> nanosheets. **d**, Scaling relationship between energy barrier and onset potential of NO<sub>3</sub>RR for pristine MoS<sub>2</sub> and M-MoS<sub>2</sub>. **e**, Projected crystal orbital Hamilton population (pCOHP) of NO adsorbed on M-MoS<sub>2</sub> nanosheets.

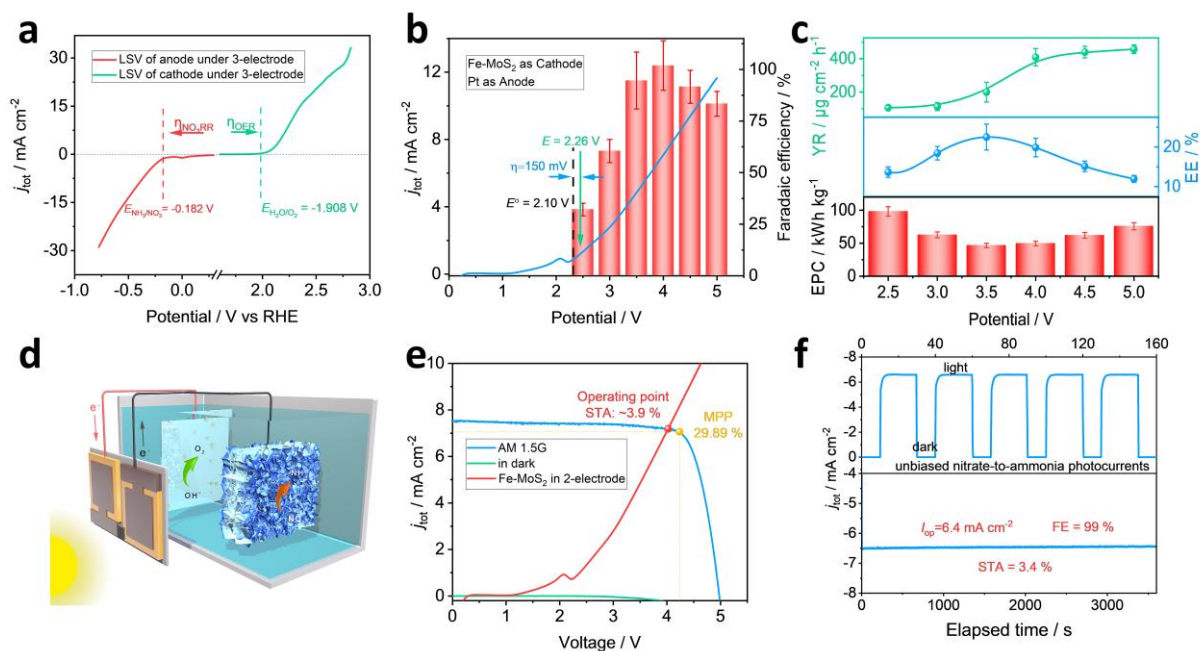


**Figure 5 | The performance of Fe-MoS<sub>2</sub> for NO<sub>3</sub>RR using a 2-electrode electrolyzer. a**, LSV curves of Fe-MoS<sub>2</sub> nanosheets and Pt used as a cathode and anode. The LSV responses were measured in a 3-electrode configuration. **b**, Polarization curve of the full cell electrolyzer with a total geometric area of  $2 \text{ cm}^2$ . **c**, Potential-dependent electric power consumption of ammonia, yield rate, and energetic conversion efficiency of the full-cell device. **d**, Schematic of the photovoltaic-electrolysis system for the conversion of nitrate to ammonia. **e**,  $J$ - $V$  characteristics of the triple junction solar under dark and simulated AM 1.5G  $100 \text{ mW cm}^{-2}$  illumination. Polarization curves of the full cell device based on Fe-MoS<sub>2</sub> nanosheets as NO<sub>3</sub>RR catalyst at the cathode. **f**, *Top*: Current density–time curve of the PV-EC system without external bias under chopped simulated AM 1.5G  $100 \text{ mW cm}^{-2}$  illumination. *Bottom*: Stability of the photocatalytic current over 1 hour.